ADVANCED FUNCTIONAL MATERIALS
www.afm-journal.de

3D Porous Metal-Scaffold Interdigitated Micro-Electrodes for High-Performance On-Chip Energy Storage Systems

*Nibagani Naresh, Yujia Fan, Yijia Zhu, Tianlei Wang, Shuhui Li, Ivan P. Parkin, Michael De Volder, and Buddha Deka Boruah**

The development of on-chip energy storage systems is essential for the next generation of System-on-Chip (SoC) technologies, particularly in powering micro-scale devices such as medical implants, micro-robots, and micro-sensors. Enhancing charge storage performance within a limited device footprint remains a key challenge, necessitating advancements in electrode design to improve energy storage capabilities. In this work, porous 3D copper (Cu) scaffold-based interdigitated electrodes (IDEs) are introduced as current collectors, where the dynamic hydrogen bubble templating (DHBT) method is employed to fabricate porous Cu scaffold IDEs, resulting in a structured porous network with increasing porosity at the top surface. This design greatly enhances the efficient loading of electrode materials of polyaniline (PANI) cathode and zinc (Zn) anode, thereby improving charge storage performance in Zn-ion micro-batteries (3D ZIMBs) and facilitating the deposition of activated carbon (AC) on 3D porous Cu for 3D micro-supercapacitors (3D MSCs). Our results demonstrate a substantial improvement in charge storage for 3D ZIMBs, achieving 32.46 μAh cm^{-2} compared to ZIMBs (PANI and Zn deposited on plane Au IDEs) with 16.99 μAh cm^{-2} at 100 μA cm^{-2}. Similarly, the 3D MSCs exhibit an areal capacitance of 22.81 mF cm^{-2} at 0.1 mA cm^{-2}, outperforming MSCs (AC deposited on plane Au IDEs) with 4.52 mF cm^{-2}. Furthermore, the 3D ZIMBs and 3D MSCs achieve impressive areal energies of 29.62 and 4.04 μWh cm^{-2}, respectively, outperforming most reported high-performance on-chip energy storage systems. Therefore, this study presents an innovative strategy to enhance the electrochemical performance of planar energy storage systems and contribute to the advancement of on-chip energy storage research.

1. Introduction

The rapid advancement of electronic miniaturization is driving the evolution of System-on-Chip (SoC) technologies, enabling the development of micro-scale devices such as medical implants, micro-robots, and micro-sensors.[1,2] On-chip micro-batteries are well-suited for high-energy applications,[3–7] whereas micro-supercapacitors (MSCs)[8–10] are more effective for delivering high-power output, depending on specific application requirements. Despite progress in developing these micro-scale energy storage devices, they still encounter challenges with the effective loading of active materials within the constrained device footprint, which hinders their charge storage performance. Since device areal size is a critical constraint in on-chip energy storage, the key challenge is how to enhance energy storage performance without increasing the overall device footprint. Equally important is the ability to enhance ion transport, maintain high electrical conductivity, and preserve structural integrity for long-term operation. To address these requirements, developing porous and periodic interdigitated electrodes (IDEs) as current collectors

N. Naresh, Y. Fan, Y. Zhu, B. D. Boruah
Institute for Materials Discovery
University College London
London WC1E 7JE, United Kingdom
E-mail: b.boruah@ucl.ac.uk

The ORCID identification number(s) for the author(s) of this article can be found under https://doi.org/10.1002/adfm.202507537

DOI: 10.1002/adfm.202507537

T. Wang, S. Li, I. P. Parkin
Department of Chemistry
University College London
London WC1H 0AJ, United Kingdom

M. De Volder
Institute for Manufacturing
Department of Engineering
University of Cambridge
Cambridge CB3 0FS, United Kingdom

is beneficial, as they enable the effective loading of active materials.[11,12] Such an electrode design is particularly beneficial for charge storage materials with intrinsically low electrical conductivity. Simply increasing material loading onto IDEs without a pre-engineered conductive framework could severely hinder ion transport, ultimately limiting performance. For instance, porous nickel (Ni) current collectors have been fabricated using the self-assembly of polystyrene (PS) templates, followed by Ni deposition and PS removal to obtain porous Ni-based current collectors for on-chip energy storage.[13–15] While this method enables the formation of well-defined porous Ni structures, the PS self-assembly process is slow, complex, and highly sensitive, necessitating the development of a more robust and scalable technique for designing porous electrode frameworks in on-chip energy storage applications.

Electrodeposition from aqueous solutions is an optimal technique, taking advantage of the aqueous electrolyte's solvent window to enable metal ion reduction without solvent decomposition. However, at high cathodic overpotential, H^+ ions are reduced to H_2 gas, disrupting metal deposition due to bubble formation. These H_2 bubbles act as dynamic templates during electrodeposition, a process known as dynamic hydrogen bubble templating (DHBT).[16] The DHBT technique offers several advantages: it eliminates the need for additional templating materials or steps, generates pores in real-time during electrodeposition, improves process efficiency, reduces material and operational costs compared to conventional templating methods, and is highly adaptable to various materials and electrode configurations. Furthermore, it is suitable for large-scale manufacturing while minimizing chemical waste by utilizing hydrogen gas as a dynamic template. Leveraging the benefits of DHBT, we employed this technique to fabricate 3D porous copper (Cu) scaffolds on Au IDEs, serving as highly efficient current collectors that enable effective loading of energy storage materials within a confined device footprint.[17,18] The resulting 3D Zn-ion micro-batteries (3D ZIMBs) incorporate zinc (Zn) as the anode and polyaniline (PANI) as the cathode, while 3D micro-supercapacitors (3D MSCs) utilize activated carbon (AC) electrodes, demonstrating how innovative porous IDE structures influence overall charge storage performance. Our results show that 3D ZIMBs achieve significantly higher areal capacities (32.54 μAh cm^{-2}) and areal energy (29.62 μWh cm^{-2}) compared to micro-batteries with plane Au IDEs, surpassing previously reported on-chip micro-supercapacitors and comparable with high-performance micro-batteries. Similarly, the 3D MSCs exhibit areal capacitance (22.81 mF cm^{-2} at 0.1 mA cm^{-2}) and areal energy (4.04 μWh cm^{-2}), exceeding the performance of most state-of-the-art MSCs. The advanced 3D IDEs not only enhance charge storage performance by providing metallic conductivity through the Cu framework and mitigating sluggish ion diffusion but also maintain consistent material morphology and structural integrity after extended cycling. The development of porous 3D metal scaffold-based IDEs with enhanced material loading capacity paves the way for the next generation of high-efficiency, durable, and secure energy storage solutions for diverse on-chip energy storage applications.

2. Results and Discussion

As illustrated in **Figure 1a**, Au IDEs were patterned onto ceramic substrates with a 200 μm gap and width, followed by the fabrication of 3D porous Cu scaffolds on the flat IDEs using DHBT through electrodeposition (detailed in the experimental section, Supporting Information). This process induces the formation of H_2 bubbles at the electrode surface, which act as soft templates, enabling the controlled deposition of porous Cu scaffolds on the Au IDEs. The resulting 3D Cu IDEs were then utilized for active material loading. Specifically, Figure 1b shows the incorporation of PANI cathodes and Zn anodes for 3D ZIMBs, while Figure 1c presents the use of AC electrodes for 3D MSCs. Digital images of the corresponding devices are displayed in Figure 1d. Detailed procedures for loading active materials onto 3D Cu IDEs and planar Au IDEs are provided in the Supporting Information. Additionally, Figure 1e,f showcases the 3D and 2D profilometer images of the fabricated 3D Cu IDEs. The profile image below reveals an electrode height of ≈26 μm, excluding the 4 μm thickness of the flat Au IDEs. These images confirm the uniform formation of the porous Cu scaffold across the Au IDEs, ensuring no short-circuiting occurred during electrodeposition using the DHBT technique. Figure 1g,h illustrates the distribution of porosity in the Cu metal scaffold through schematic representations. During electrodeposition at a relatively high current of −1 A, the evolution of H_2 bubbles influences the formation of the porous Cu film, where the reduction reactions drive the deposition process. It is evident that smaller pores initially form near the electrode surface, while larger pores emerge as the film extends outward. This pattern is clearly visible in SEM surface images (Figure 1i,j), where a layered structure can be observed in smaller underlying pores positioned beneath larger upper pores. The progressive growth in pore size can be attributed to the gradual merging of H_2 bubbles. Initially, tiny bubbles coalesce within constrained spaces, but as deposition progresses, morphological changes encourage the expansion of larger voids. This process follows a "layered growth" model, where the initial phase produces narrower pores, followed by the development of broader pores as the scaffold extends perpendicularly.[15] The cross-sectional SEM images (Figure 1i,j) further validate this porosity distribution, revealing a clear distinction between larger pores concentrated at the top and smaller pores predominant at the lower regions of the scaffold. Additionally, Figure 1k–n displays top-view SEM images of the porous Cu scaffold at varying magnifications, showcasing a distinct nanowire-like morphology. These images further confirm the uniform deposition of the Cu scaffold on Au IDEs, ensuring no short-circuiting between electrodes occurs during electrodeposition. Moreover, the Cu nanowire-like morphology significantly enhances the surface area, providing an advantage for the efficient loading of active energy materials. This feature is particularly beneficial for electrodeposition-based material loading, as the expanded surface offers numerous active sites, improving material integration and boosting overall energy storage performance.

To fabricate 3D ZIMBs, Zn (anode) and PANI (cathode) were deposited onto 3D Cu IDEs using Microplotter and electrodeposition techniques. To better understand the influence of the 3D metal scaffold on charge storage performance, a comparative

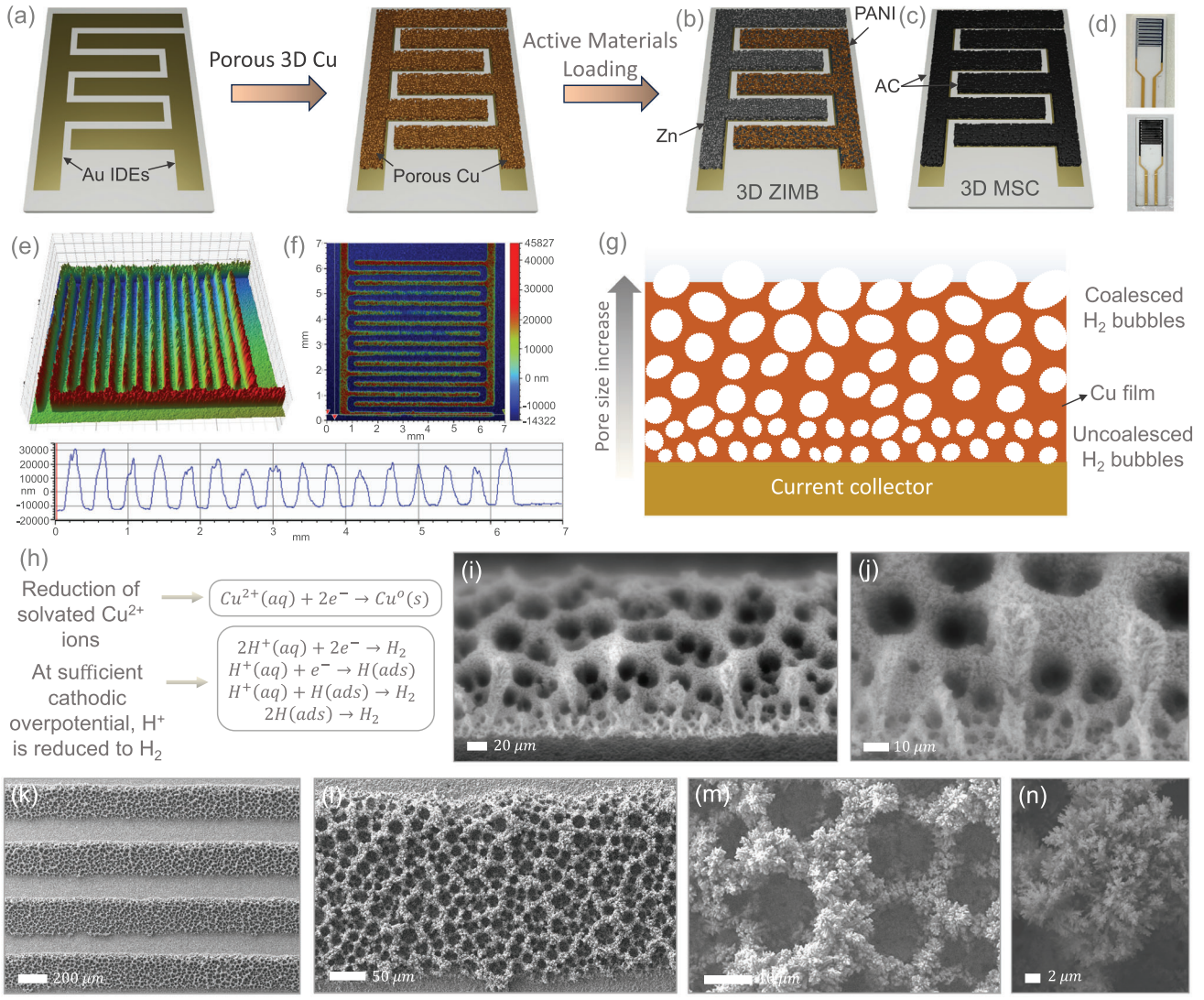

Figure 1. a) Schematic representation of the fabrication steps for Cu metal scaffold-based IDE current collectors, incorporating the DHBT method, followed by active material loading to fabricate b) a 3D ZIMB with a PANI cathode and Zn anode, and c) a 3D MSC with AC electrodes. d) Digital photographs of the 3D ZIMB (top) and 3D MSC (bottom). e,f) 3D and 2D profilometer images of the 3D Cu IDEs, with the lower image showing electrode height profiles, measuring ≈26 µm, excluding a flat Au IDEs thickness of ≈4 µm. g) Schematic depiction of porosity evolution in the Cu metal scaffold, where increasing thickness leads to greater porosity due to the coalescence of H_2 bubbles, forming larger pores. h) Illustration of the reduction reactions occurring during Cu metal scaffold deposition on Au IDEs at relatively high cathodic overpotential. i,j) Cross-sectional SEM images of the porous Cu metal scaffold at low and high magnifications, show porosity distribution, with increasing porosity toward the top. k–n) Top-view SEM images of the porous Cu metal scaffold at various magnifications, highlighting nanowire-like Cu morphologies.

study was conducted by depositing both PANI and Zn onto planar Au IDEs (ZIMB) (as described in the experimental section of the Supporting Information). The SEM images captured at various magnifications (**Figure** 2a–i) confirm the successful deposition of Zn and PANI onto the porous Cu scaffold. The PANI cathode was incorporated using the electrodeposition technique, while Zn nanoparticles were loaded via the Microplotter technique. As shown in Figure 2d–f, Zn nanoparticles were effectively deposited onto the porous Cu metal scaffold without compromising its original structure. The high-magnification SEM image of the Zn anode (Figure 2f) demonstrates a uniform distribution of Zn nanoparticles, attributed to the high precision of the Microplotter technique. Similarly, SEM images of the PANI cathode at different magnifications (Figure 2g–i) illustrate its successful incorporation into the porous Cu scaffold. As seen in Figure 2g, PANI fully coats the porous Cu metal scaffold without any cracks or damage, achieved through optimized electrodeposition parameters. The high-resolution SEM image of electrodeposited PANI (Figure 2i) reveals a nanowire-like morphology with distinct porosity. The EDS mapping images of 3D ZIMB (see Figures S1 and S2, Supporting Information) confirm the uniform distribution of C and N elements within the PANI electrode. Similarly, they confirm the uniform distribution of Zn throughout the anode (Zn electrode). The SEM images of the ZIMB device (refer to

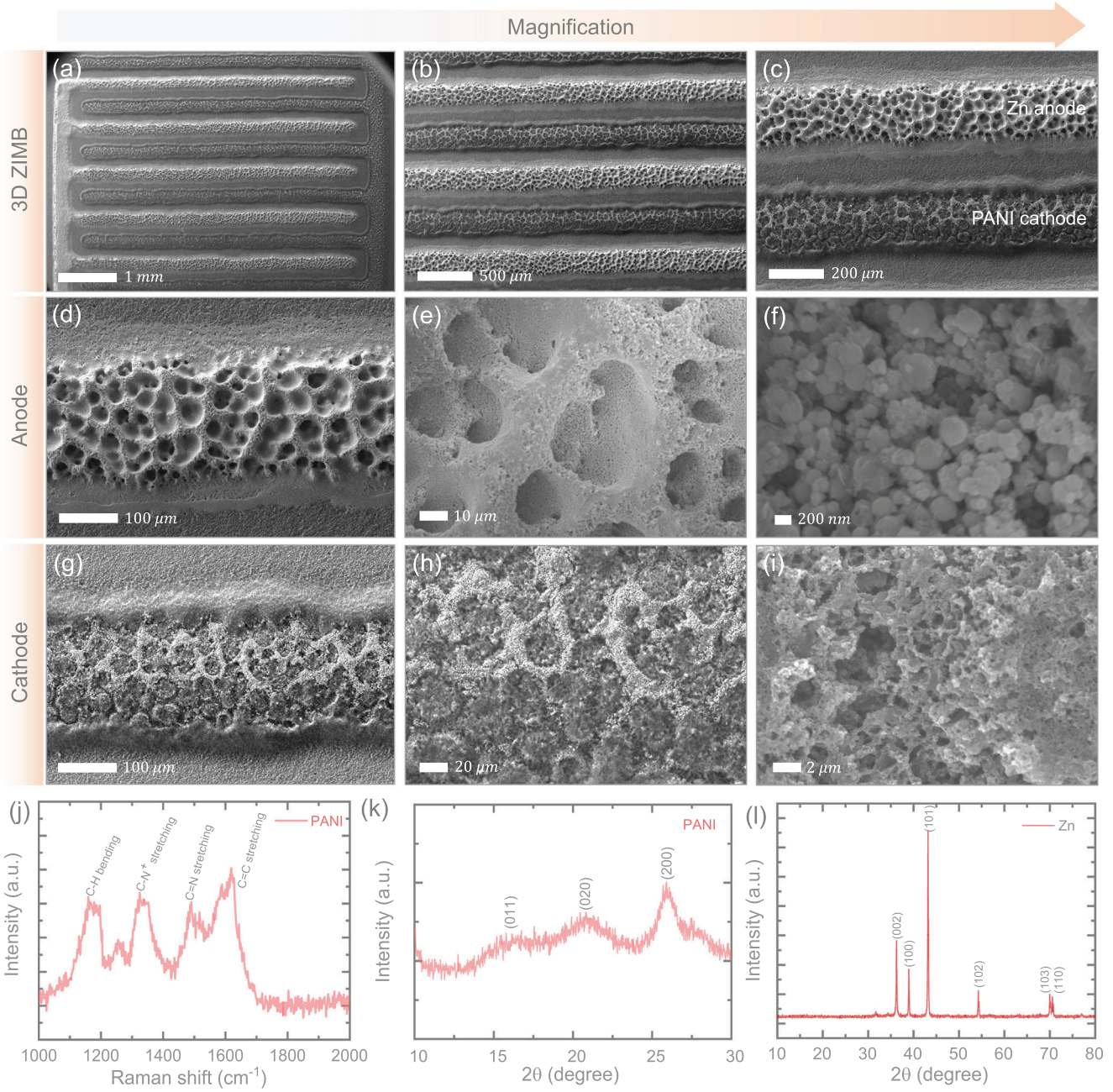

Figure 2. a–c) SEM images of 3D ZIMB at different magnifications, demonstrating the successful loading of active materials onto the porous Cu scaffold IDEs. d–f) SEM images of the loaded Zn anode using the Microplotter technique at different magnifications, showing the Zn nanoparticles are decorated with Cu scaffold networks. g–i) Further magnified images of the PANI cathode process using the electrodeposition technique, showing full coverage with PANI. The further magnified images reveal that the PANI has a nanowire-like morphology with distinct porosities, potentially increasing effective interaction with the electrolyte and interfaces. j,k) Raman and XRD patterns of electrodeposited PANI. l) XRD patterns of the used Zn nanoparticles.

Figure S3, Supporting Information) confirm the successful deposition of PANI and Zn on planar Au IDEs. The high-resolution SEM images also display a nanowire-like morphology of PANI and Zn nanoparticles. Additionally, Figure S4 (Supporting Information) showcases the 3D and 2D profilometer images of the fabricated 3D ZIMB and ZIMB. These images further confirm the uniform deposition of PANI and Zn throughout the porous Cu scaffold across the Au IDEs, ensuring no short-circuiting occurred. The structural characterization of electrodeposited PANI and Microplotted Zn nanoparticles was investigated using Raman spectroscopy and XRD analysis, as shown in Figure 2j–l. The Raman spectrum of PANI (Figure 2j) exhibits characteristic peaks at 1169, 1330, 1490, and 1617 cm^{-1}, corresponding to C—H bending, C—N^+ stretching, C=N stretching, and C=C stretching modes, respectively.[19] The XRD pattern of PANI (Figure 2k) reveals broad crystalline peaks within an amorphous matrix, with

characteristic peaks at 16.04°, 20.84°, and 25.94°, corresponding to the (011), (020), and (200) planes.[20] Similarly, the XRD pattern of Zn nanoparticles (Figure 2l) exhibits highly crystalline peaks at 36.28°, 39.10°, 43.14°, 54.33°, 70.07°, and 70.74°, corresponding to the (002), (100), (101), (102), (103), and (110) planes of hexagonal Zn, referencing PDF#87-0713.[21]

Next, the charge storage performance of both ZIMBs and 3D ZIMBs was evaluated using a gel electrolyte composed of 3M $Zn(CF_3SO_3)_2$ in PVA (see the experimental section for details on electrolyte composition). Electrochemical measurements were conducted by immersing the micro-batteries in the gel electrolyte within a cuvette (Figure S5, Supporting Information). **Figure 3**a presents the comparative cyclic voltammetry (CV) curves of ZIMB and 3D ZIMB recorded at a scan rate of 0.3 mV s^{-1} over a voltage range of 0.5–1.5 V. Both systems exhibit distinct pairs of redox peaks, which correspond to the interaction of Zn^{2+} ions during the charge storage process. The charge storage mechanism involves conjugated (C═N) bonds, which facilitate anion binding with oxidized PANI (C—N^+), while cations are stored at reduced PANI (C—N^-) sites.[22,23] Specifically, in this system, the triflate anion ($CF_3SO_3^-$) interacts with oxidized PANI during the charge state, whereas Zn^{2+} binds to reduced PANI during the discharge state. A schematic illustration (Figure 3b) further elucidates the changes in PANI oxidation states during charge storage, as well as the interaction of Zn^{2+} and $CF_3SO_3^-$ in their respective states.[22] Notably, the area under the CV curves of 3D ZIMB, compared to ZIMB, demonstrates a significant enhancement in charge storage performance, despite both systems being tested under the same experimental conditions. To further evaluate the electrolyte stability of the 3D porous Cu IDEs, a device was fabricated with Zn (anode) micro-plotted onto one side of the 3D porous Cu IDE, while the other side remained as pristine 3D porous Cu. Electrochemical tests were conducted using the same gel electrolyte. As shown in Figure S6 (see Supporting Information), the CV curve of the porous Cu device displays a negligible oxidation peak in comparison to the 3D ZIMB device. This is likely due to the fact that, in 3D ZIMBs, both the cathode (PANI) and anode (Zn) almost completely cover the porous 3D Cu current collectors, minimizing redox activity from the Cu substrate. Moreover, the capacity improvement is further validated by galvanostatic discharge-charge (GDC) profiles recorded at various areal currents ranging from 100 to 1000 μA cm^{-2} over a voltage range of 0.5–1.5 V (Figure 3c,d). At an areal current of 100 μA cm^{-2}, the measured areal capacities for ZIMB and 3D ZIMB are 16.79 and 32.43 μAh cm^{-2}, respectively (Figure 3e), highlighting the substantial impact of the 3D porous scaffold in enhancing charge storage performance compared to planar IDEs. The electrochemical impedance spectroscopy (EIS) analysis of both systems (Figure 3f) further supports these findings. Despite achieving higher capacities, the 3D ZIMB also exhibits lower charge transfer resistance compared to ZIMB. Additionally, the Nyquist plot at lower frequency regions indicates enhanced Zn^{2+} diffusion kinetics, as demonstrated by the steeper slope of the Warburg region, suggesting better performance at higher operational rates. Figure 3g illustrates the comparative rate capability of ZIMB and 3D ZIMB across different areal currents, further confirming the improved charge storage performance of 3D ZIMB at every tested condition. For example, at 200 and 500 μA cm^{-2}, the measured areal capacities for ZIMB are 15.51 and 9.53 μAh cm^{-2}, which increase to 28.78 and 16.39 μAh cm^{-2} in 3D ZIMB, respectively. Moreover, Figure S7 (Supporting Information) highlights that the 3D ZIMB delivers notably higher volumetric capacities compared to the planar ZIMB at lower areal currents (100–400 μA cm^{-2}), while sustaining comparable performance even at elevated areal current (1000 μA cm^{-2}), further emphasizing the effectiveness of the Cu scaffold-based IDE current collector design.

To evaluate the long-term cycling stability of the ZIMB and 3D ZIMB, GDC tests were conducted for 200 cycles, as shown in **Figures** 4a and S8 (Supporting Information). The results indicate consistent performance throughout cycling, with capacity retentions of 89.98% and 70.83% after 200 cycles for ZIMB and 3D ZIMB, respectively, while both systems maintained a coulombic efficiency of ≈99.9%. Figure S9 (Supporting Information) presents digital images of a 3D ZIMB before and after long-term cycling. To further investigate the materials stability of the micro-electrodes, ex-situ SEM and Raman analyses were performed on the cycled devices. Figure 4b–g presents post-mortem SEM images of the cycled 3D ZIMB, with low-magnification images (Figure 4b) confirming that no short-circuiting occurred even after extended cycling. The high-magnification SEM images of the Zn anode (Figure 4c,d) reveal a stable 3D anode, with no significant cracks throughout the micro-electrode. However, minor fractures were detected, likely caused by stress accumulation during repetitive cycling. Notably, no significant dendritic Zn growth was observed at the edges of the 3D Zn anode, instead, localized Zn plating was identified in certain regions of the 3D Zn micro-anode (inset in Figure 4d). The cycled 3D PANI micro-cathode exhibited a well-preserved morphology, retaining its nanowire-like structure without significant cracking (Figure 4g, inset). Although minor cracks were observed on the 3D micro-electrodes, there was no material delamination from the porous 3D Cu IDEs, which provides an additional advantage. The structural integrity of our porous 3D Cu IDEs not only enables efficient loading of electrode materials (PANI and Zn in this case) but also ensures strong material adhesion, effectively minimizing material detachment and enhancing electrode durability over extended cycles. The ex-situ Raman analysis of the PANI cathodes before and after cycling is presented in Figure 4h. The characteristic Raman peaks of the cycled PANI cathodes remain identical to those observed before cycling, indicating that the stability of PANI is well-preserved even after prolonged cycling. This stability makes it a promising candidate for Zn-ion storage, particularly in micro-battery designs. Moreover, the functionality of the 3D ZIMB was demonstrated by successfully powering commercial sensors. As illustrated in Figure 4i, two fully charged 3D ZIMBs connected in series effectively powered an indoor-outdoor thermometer with a hygrometer clock, highlighting the potential for broader applications of on-chip micro-batteries.

To further demonstrate the novelty of our porous Cu IDEs and their potential for on-chip energy storage, we fabricated 3D MSCs using AC electrodes, which facilitate efficient electrical double-layer capacitance. For precise and effective loading of AC materials, we employed the Microplotter technique, following a process reported previously by our research group,[24,25] enabling selective deposition of AC onto the confined IDEs. To ensure a fair comparison of charge storage performance, we loaded AC materials onto both 3D porous Cu IDEs (3D MSCs) and planar Au

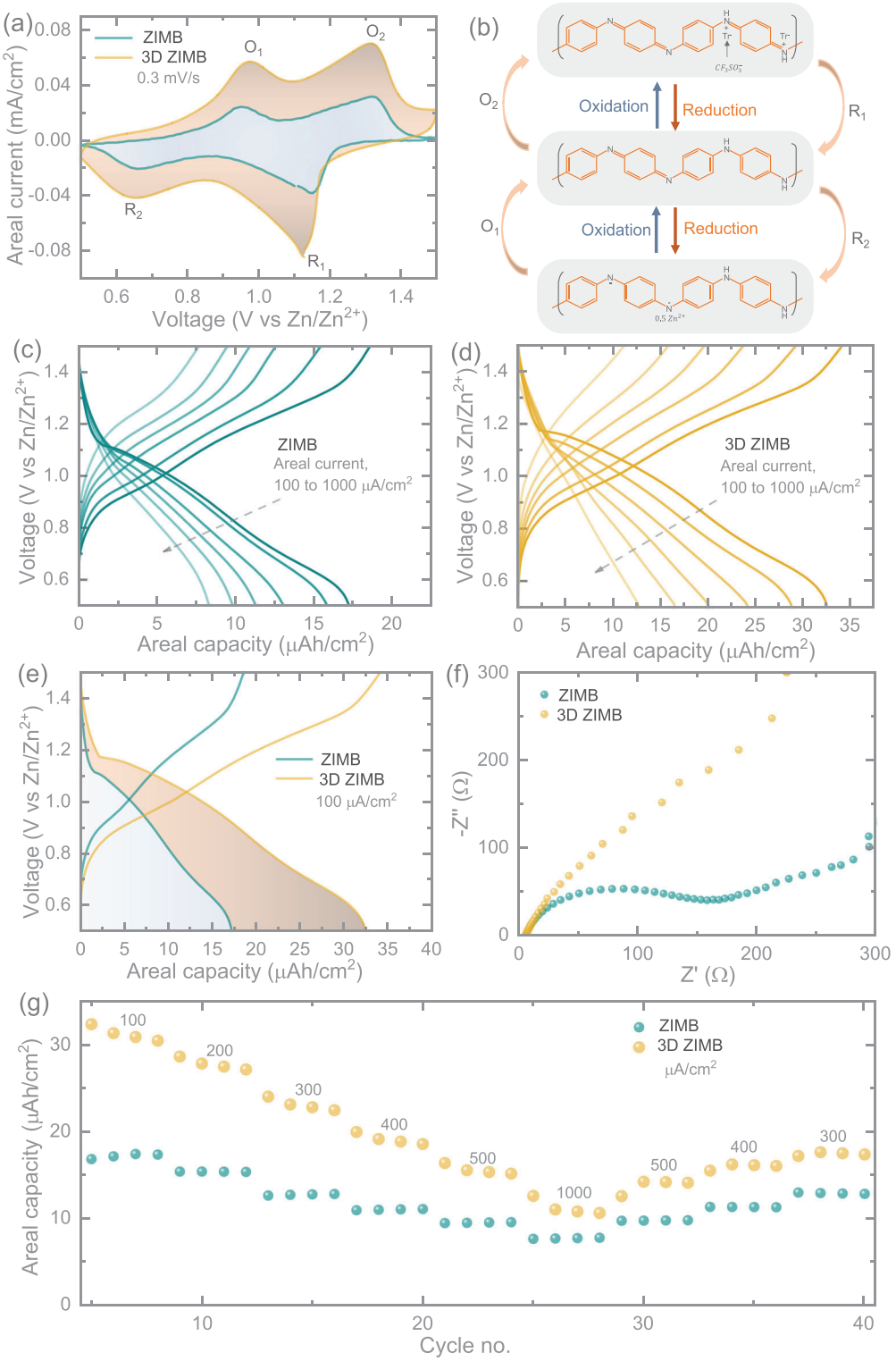

Figure 3. a) Comparative CVs of ZIMB and 3D ZIMB recorded at a scan rate of 0.3 mV s^{-1} within a voltage range of 0.5 to 1.5 V. b) Schematic representation of the hybrid charge storage mechanism in the PANI cathode. c,d) GDC profiles of ZIMB and 3D ZIMB at various areal currents ranging from 100 to 1000 μA cm^{-2} over the same voltage window. e) Comparative GDC curves of both micro-batteries were measured at an areal current of 100 μA cm^{-2}. f) Nyquist plots illustrate the electrochemical impedance characteristics of ZIMB and 3D ZIMB. g) Rate performance evaluation of ZIMB and 3D ZIMB across different areal currents, progressively increasing from 100 to 1000 μA cm^{-2}, followed by a return to 300 μA cm^{-2}.

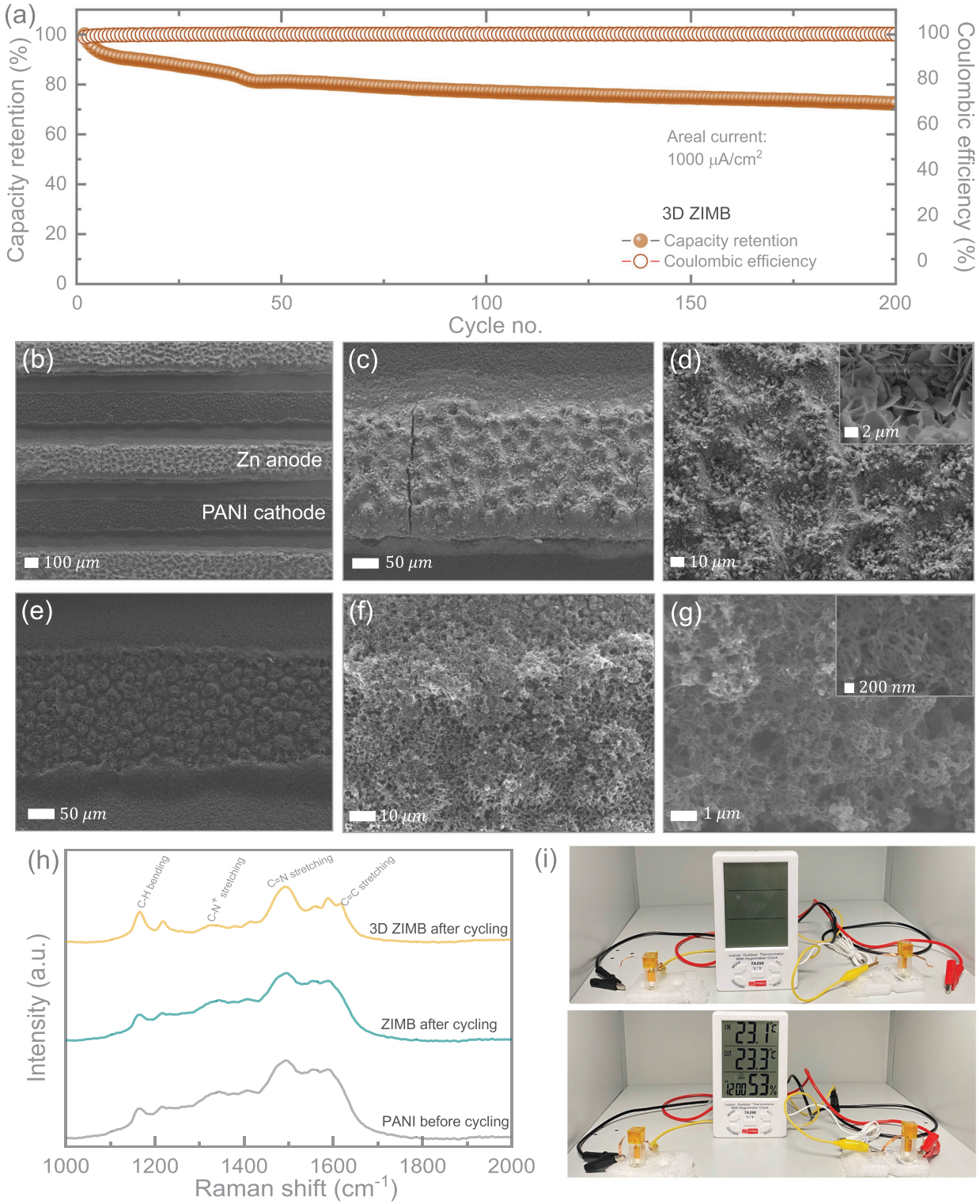

Figure 4. a) Long-term cycling performance of the 3D ZIMB over 200 cycles, showing a capacity retention of ≈70.83% and a coulombic efficiency close to 100%. b) Post-cycling SEM image of the 3D ZIMB after extended operation. c,d) SEM images of the cycled Zn anode at low and high magnifications. e–g) Post-cycling SEM images of the PANI cathode were captured at different magnifications to assess morphological integrity. h) Raman spectra comparing the pristine and cycled PANI cathodes. i) Demonstration of two 3D ZIMBs connected in series to power an indoor-outdoor thermometer with a hygrometer clock.

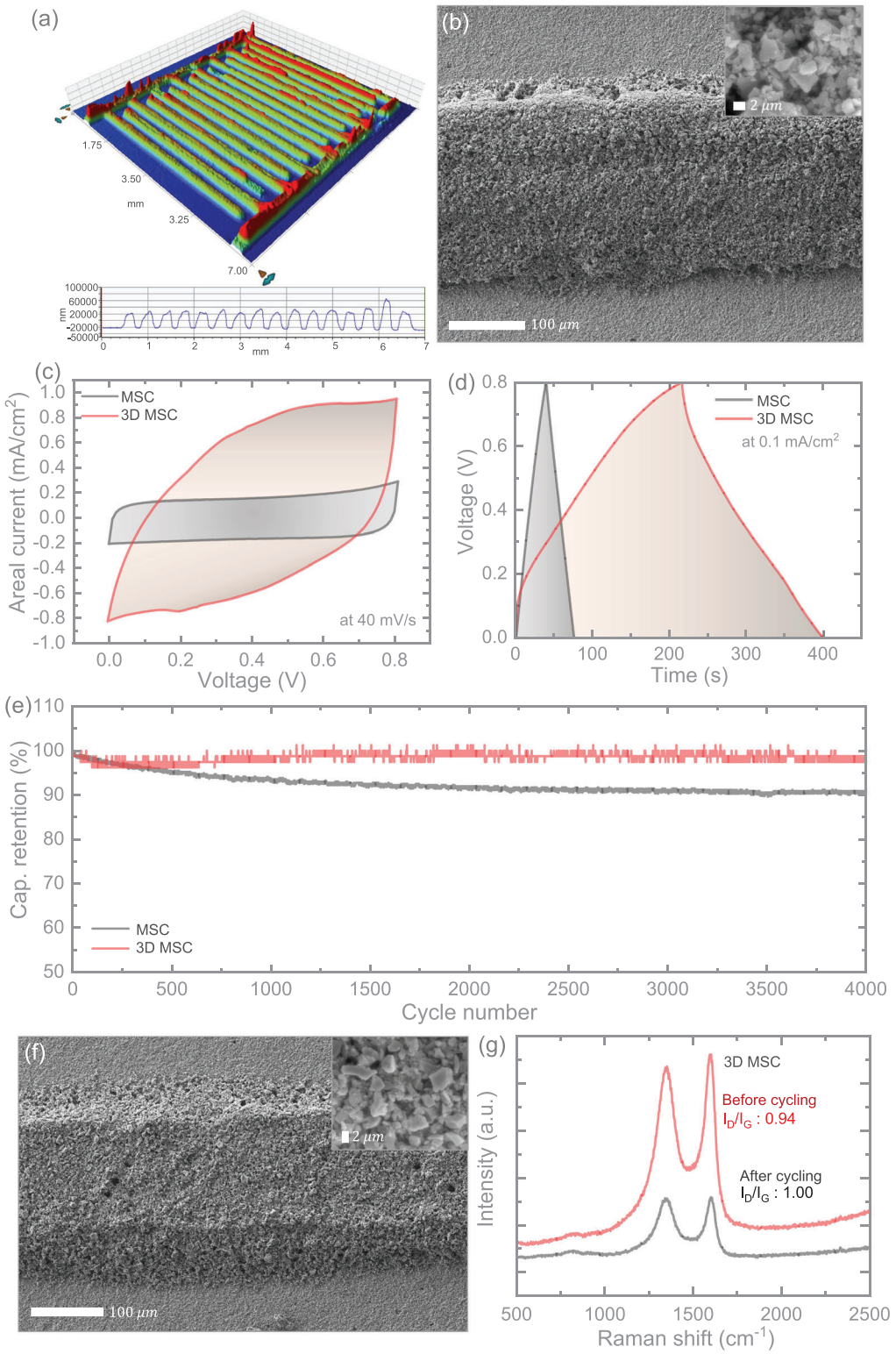

Figure 5. a) 3D profilometer image of the 3D MSC, with the plot below displaying the height profile of the IDEs, showing an average electrode height of ≈36 µm, excluding the flat Au IDEs thickness of ≈4 µm. b) SEM images of the AC electrode at various magnifications, demonstrating the uniform distribution of AC particles on the 3D Cu scaffold IDE. c) Comparative CV curves at 40 mV s^{-1} and d) GCD curves at 0.1 mA cm^{-2} for both MSC and 3D MSC. e) Long-term cycling performance of MSC and 3D MSC over 4000 cycles, with capacity retention of ≈90.75% for MSC and ≈98.41% for 3D MSC. f) Post-cycling SEM images of the 3D MSC at different magnifications, where the high-magnification image confirms the preserved AC structure even after extended cycling. g) Raman spectra of the AC electrodes in 3D MSC before and after cycling, illustrating material stability.

IDEs (MSC) and compared their electrochemical behavior. Digital images, profilometer images, and SEM images of the MSCs are provided in Figures S10 and S11 (Supporting Information). **Figure** 5a shows a 3D profilometer image of the 3D MSC, illustrating an average electrode height of ≈36 µm, excluding the flat Au IDEs thickness of ≈4 µm. Figure 5b displays an SEM image of the AC electrode, with the inset showing a high-magnification view. Additional low-magnification SEM images of 3D MSC are available in the Supporting Information (Figure S12, Supporting Information). Figure S13 (Supporting Information) presents the XRD pattern of the utilized AC electrode material. For electrochemical testing, we employed a H_3PO_4/PVA gel electrolyte and evaluated performance over a voltage window of 0–0.8 V. The CV curves of MSC and 3D MSC at different scan rates (10–100 mV s^{-1}) are provided in Figure S14 (Supporting Information). The nearly rectangular shape of the CVs, without distinct redox peaks, confirms the electrical double-layer charge storage behavior in symmetric AC electrodes. Similarly, the triangular-shaped galvanostatic charge-discharge (GCD) curves (Figure S15, Supporting Information) at various areal currents (0.1–1.0 mA cm^{-2}) further validate the double-layer capacitive characteristics. Additionally, the area under the CV curves of 3D MSC is significantly larger than that of MSC at the same scan rates. For instance, at 40 mV s^{-1}, an improvement of ≈321% in the area under the CV curve was observed in 3D MSC compared to MSC (Figure 5c), demonstrating a notable enhancement in charge storage performance. Likewise, the extended charge-discharge duration in the GCD plot (Figure 5d) at an areal current of 0.1 mA cm^{-2} further supports capacitance enhancement. The calculated areal capacitances for MSC and 3D MSC were determined to be 4.525 and 22.73 mF cm^{-2}, respectively. At all tested areal currents, 3D MSC consistently exhibited higher areal capacitances than MSC (Figure S16, Supporting Information), ultimately leading to superior areal energy storage after incorporating the 3D Cu scaffold-based IDEs.

Furthermore, the long-term cycling stability of both MSC and 3D MSC was evaluated over 4000 cycles, as shown in Figure 5e. Notably, the 3D MSC not only exhibited higher charge storage performance but also demonstrated greater capacitance stability throughout extended cycling. The measured capacitance retention after 4000 cycles was 90.75% for MSC and 98.41% for 3D MSC, highlighting the enhanced durability of the 3D electrode architecture. To further assess the morphological integrity of the electrodes after cycling, post-mortem SEM analysis was conducted. The results confirmed that even after prolonged cycling, the AC electrodes retained their original geometry and morphology, as observed in Figure 5f and Figure S17 (Supporting Information). A similar morphological consistency was observed in the MSC after cycling, as shown in Figure S18 (Supporting Information). This stability is attributed to the electrical double-layer charge storage mechanism of the high-surface-area AC particles, which ensures minimal degradation. The measured surface area of AC particles was determined to be 1586 m^2 g^{-1}.[24] Additionally, Raman spectroscopy of the AC particles before and after cycling, presented in Figure 5g, demonstrates that the characteristic D and G bands remained distinct even after extended cycling. However, a slight increase in defect peak intensity was observed, with the I_D/I_G intensity ratio increasing from 0.94 to 1.00. This slight shift suggests the formation of surface-related defects on the AC particles, likely due to cycling-induced modifications.

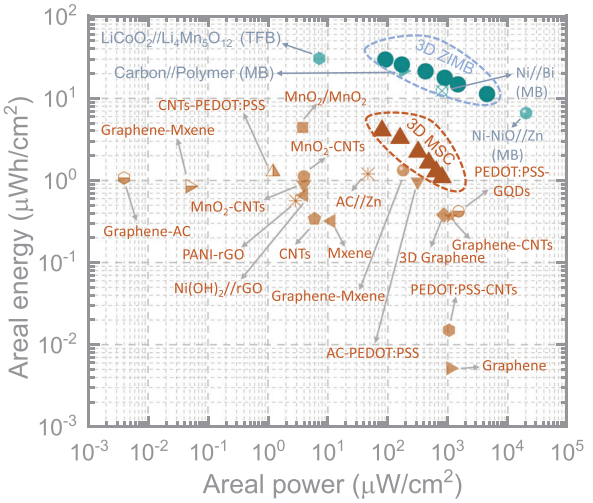

Figure 6. Ragone plot comparing the areal energy and areal power performance of the 3D ZIMB and 3D MSC with previously reported micro-supercapacitors both in symmetric design, asymmetric design and micro-batteries: graphene,[26] PEDOT:PSS-CNTs,[27] 3D graphene,[28] Mxene,[29] CNTs,[30] graphene CNTs,[31] MnO_2-CNTs//V_2O_5-CNTs,[32] $Ni(OH)_2$//rGO,[33] AC-PEDOT:PSS,[25] graphene-Mxene,[34,35] CNTs-PEDOT:PSS,[36] PEDOT-PSS:GQDs,[37] PANI-rGO,[38] graphene-AC,[39] MnO_2,[40] MnO_2-CNTs,.[41] The 3D ZIMB exhibits energy storage characteristics comparable to high-performance micro-batteries: carbon//polymer,[42] Ni-NiO//Zn,[43] Ni//Bi,[44] thin-film batteries: $LiCoO_2$//$Li_4Mn_5O_{12}$,[45] highlighting its potential for advanced on-chip energy storage applications.

Next, we evaluate the areal energy and areal power of our 3D ZIMBs and 3D MSCs in comparison with previously reported micro-supercapacitors and micro-batteries, as presented in the Ragone plot (**Figure 6**). The results indicate that our 3D MSCs achieve peak areal energy and peak areal power of 4.04 µWh $cm^{-2}$and 800 µW cm^{-2}, respectively, surpassing most reported micro-supercapacitors, including both symmetric and asymmetric electrode designs. Notably, the 3D ZIMBs not only exhibit higher areal energies, as expected based on their charge storage mechanism but also demonstrate comparable or even superior areal powers compared to high-performance micro-supercapacitors. The measured peak areal energy and peak areal power for 3D ZIMBs are 29.62 µWh cm^{-2} and 4502 µW cm^{-2}, respectively. Furthermore, our 3D ZIMBs deliver energy storage performance comparable to that of previously reported micro-batteries and thin-film batteries (Figure 6). These findings highlight the strength of our advanced micro-electrode architecture in delivering enhanced charge storage within a miniaturized footprint. This work paves the way for high-performance on-chip energy storage systems, which are vital for the continued evolution of smart system-on-chip technologies.

This study explores the use of porous 3D Cu scaffold-based IDEs, fabricated through the DHBT method, as current collectors for micro-energy storage devices. These porous electrodes enable efficient loading of active materials, resulting in enhanced energy storage within the compact footprints of 3D ZIMBs and 3D MSCs. Our results show that the 3D ZIMBs achieve a signifi-

cantly higher areal capacity of 32.46 μAh cm^{-2} compared to 16.99 μAh cm^{-2} for ZIMBs at a current density of 100 μA cm^{-2}. Similarly, the 3D MSCs demonstrate an areal capacitance of 22.81 mF cm^{-2} at 0.1 mA cm^{-2}, far exceeding the 4.52 mF cm^{-2} of standard MSCs. Additionally, the 3D ZIMBs and 3D MSCs exhibit impressive areal energy densities of 29.62 and 4.04 μWh cm^{-2}, respectively, outperforming many high-performance on-chip energy storage devices. Therefore, this research presents a novel strategy to enhance electrochemical efficiency in planar microenergy storage devices, paving the way for future SoC electronic applications.

Supporting Information

Supporting Information is available from the Wiley Online Library or from the author.

Acknowledgements

B.D.B. acknowledges support from the EPSRC research grant EP/Y008103/1, B.D.B. and M.D.V. acknowledge support from the EPSRC research grant EP/Y008332/1.

Conflict of Interest

The authors declare no conflict of interest.

Data Availability Statement

The data that support the findings of this study are available from the corresponding author upon reasonable request.

Keywords

3D porous copper scaffold, dynamic hydrogen bubble templating, high-performance, on-chip energy storage

Received: April 2, 2025
Revised: April 26, 2025
Published online:

[1] Q. Xia, F. Zan, Q. Zhang, W. Liu, Q. Li, Y. He, J. Hua, J. Liu, J. Xu, J. Wang, C. Wu, H. Xia, *Adv. Mater.* **2023**, *35*, 1.
[2] P. Li, M. Liao, J. Li, L. Ye, X. Cheng, B. Wang, H. Peng, *Small Struct.* **2022**, *3*, 1.
[3] C. Dai, L. Hu, X. Jin, Y. Wang, R. Wang, Y. Xiao, X. Li, X. Zhang, L. Song, Y. Han, H. Cheng, Y. Zhao, Z. Zhang, F. Liu, L. Jiang, L. Qu, *Sci. Adv.* **2022**, *8*, 1.
[4] X. Jin, L. Song, C. Dai, Y. Xiao, Y. Han, X. Li, Y. Wang, J. Zhang, Y. Zhao, Z. Zhang, N. Chen, L. Jiang, L. Qu, *Adv. Mater.* **2022**, *34*, 1.
[5] S. Zheng, X. Shi, P. Das, Z. S. Wu, X. Bao, *Adv. Mater.* **2019**, *31*, 1.
[6] Z. Qu, M. Zhu, Y. Yin, Y. Huang, H. Tang, J. Ge, Y. Li, D. D. Karnaushenko, D. Karnaushenko, O. G. Schmidt, *Adv. Energy Mater.* **2022**, *12*, 2200714.
[7] Y. Liu, S. Zheng, J. Ma, X. Wang, L. Zhang, P. Das, K. Wang, Z. S. Wu, *Adv. Energy Mater.* **2022**, *12*, 1.
[8] B. D. Boruah, *Energy Storage Mater.* **2019**, *21*, 219.
[9] Q. M. Saqib, A. Mannan, M. Noman, M. Y. Chougale, C. S. Patil, Y. Ko, J. Kim, S. R. Patil, M. Yousuf, R. Ali Shaukat, Y. Pyo Jeon, D. Dubal, J. Bae, *Chem. Eng. J.* **2024**, *490*, 151857.
[10] J. Zhang, G. Zhang, T. Zhou, S. Sun, *Adv. Funct. Mater.* **2020**, *30*, 1.
[11] P. Zhang, Y. Li, M. Gao, S. Yang, M. Wang, Z. Liu, K. Guo, F. Wang, X. Lu, *Chem. Eng. J.* **2023**, *454*, 140357.
[12] P. Zhang, S. Yang, H. Xie, Y. Li, F. Wang, M. Gao, K. Guo, R. Wang, X. Lu, *ACS Nano* **2022**, *16*, 17593.
[13] J. H. Pikul, H. Gang Zhang, J. Cho, P. V. Braun, W. P. King, *Nat. Commun.* **2013**, *4*, 1.
[14] Z. Liu, X. Yuan, S. Zhang, J. Wang, Q. Huang, N. Yu, Y. Zhu, L. Fu, F. Wang, Y. Chen, Y. Wu, *NPG Asia Mater.* **2019**, *11*, 12.
[15] Z. Hao, L. Xu, Q. Liu, W. Yang, X. Liao, J. Meng, X. Hong, L. He, L. Mai, *Adv. Funct. Mater.* **2019**, *29*, 1.
[16] B. J. Plowman, L. A. Jones, S. K. Bhargava, *Chem. Commun.* **2015**, *51*, 4331.
[17] N. Naresh, Y. Zhu, J. Luo, Y. Fan, T. Wang, K. Raju, M. De Volder, I. P. Parkin, B. D. Boruah, *Adv. Funct. Mater.* **2024**, *35*, 2413777.
[18] N. Naresh, Y. Zhu, Y. Fan, J. Luo, T. Wang, I. P. Parkin, B. D. Boruah, *Nano Lett.* **2024**, *24*, 11059.
[19] M. Trchová, Z. Morávková, M. Bláha, J. Stejskal, *Electrochim. Acta* **2014**, *122*, 28.
[20] M. Mitra, C. Kulsi, K. Chatterjee, K. Kargupta, S. Ganguly, D. Banerjee, S. Goswami, *RSC Adv.* **2015**, *5*, 31039.
[21] P. Zhang, Y. Li, G. Wang, F. Wang, S. Yang, F. Zhu, X. Zhuang, O. G. Schmidt, X. Feng, *Adv. Mater.* **2019**, *31*, 1.
[22] F. Wan, L. Zhang, X. Wang, S. Bi, Z. Niu, J. Chen, *Adv. Funct. Mater.* **2018**, *28*, 1.
[23] P. Jiménez, E. Levillain, O. Alévêque, D. Guyomard, B. Lestriez, J. Gaubicher, *Angew. Chemie.– Int. Ed.* **2017**, *56*, 1553.
[24] Y. Fan, I. Pinnock, X. Hu, T. Wang, Y. Lu, R. Li, M. Wang, I. P. Parkin, M. De Volder, B. D. Boruah, *Nano Lett.* **2024**, *24*, 10874.
[25] Y. Fan, T. Wang, R. Asrosa, B. Li, N. Naresh, X. Liu, S. Guan, R. Li, M. Wang, I. P. Parkin, B. D. Boruah, *Chem. Eng. J.* **2024**, *488*, 150672.
[26] L. Li, E. B. Secor, K. S. Chen, J. Zhu, X. Liu, T. Z. Gao, J. W. T. Seo, Y. Zhao, M. C. Hersam, *Adv. Energy Mater.* **2016**, *6*, 1.
[27] W. Liu, C. Lu, H. Li, R. Y. Tay, L. Sun, X. Wang, W. L. Chow, X. Wang, B. K. Tay, Z. Chen, J. Yan, K. Feng, G. Lui, R. Tjandra, L. Rasenthiram, G. Chiu, A. Yu, *J. Mater. Chem. A* **2016**, *4*, 3754.
[28] L. Zhang, D. DeArmond, N. T. Alvarez, R. Malik, N. Oslin, C. McConnell, P. K. Adusei, Y. Y. Hsieh, V. Shanov, *Small* **2017**, *13*, 1.
[29] M. Kunitski, N. Eicke, P. Huber, J. Köhler, S. Zeller, J. Voigtsberger, N. Schlott, K. Henrichs, H. Sann, F. Trinter, L. P. H. Schmidt, A. Kalinin, M. S. Schöffler, T. Jahnke, M. Lein, R. Dörner, *Nat. Commun.* **2019**, *10*, 1.
[30] H. Kim, J. Yoon, G. Lee, S. H. Paik, G. Choi, D. Kim, B. M. Kim, G. Zi, J. S. Ha, *ACS Appl. Mater. Interfaces* **2016**, *8*, 16016.
[31] S. Bellani, E. Petroni, A. E. Del Rio Castillo, N. Curreli, B. Martín-García, R. Oropesa-Nuñez, M. Prato, F. Bonaccorso, *Adv. Funct. Mater.* **2019**, *29*, 1.
[32] J. Yun, Y. Lim, H. Lee, G. Lee, H. Park, S. Y. Hong, S. W. Jin, Y. H. Lee, S. S. Lee, J. S. Ha, *Adv. Funct. Mater.* **2017**, *27*, 1.
[33] G. Huang, N. Li, Y. Du, Q. Feng, H. Xiao, X. Wu, *ACS Appl. Mater. Interfaces* **2018**, *10*, 723.
[34] Y. Yue, N. Liu, Y. Ma, S. Wang, W. Liu, C. Luo, H. Zhang, F. Cheng, J. Rao, X. Hu, J. Su, Y. Gao, *ACS Nano* **2018**, *12*, 4224.
[35] H. Li, Y. Hou, F. Wang, M. R. Lohe, X. Zhuang, L. Niu, X. Feng, *Adv. Energy Mater.* **2017**, *7*, 1.
[36] H. Xiao, Z. S. Wu, F. Zhou, S. Zheng, D. Sui, Y. Chen, X. Bao, *Energy Storage Mater.* **2018**, *13*, 233.
[37] Z. Li, V. Ruiz, V. Mishukova, Q. Wan, H. Liu, H. Xue, Y. Gao, G. Cao, Y. Li, X. Zhuang, J. Weissenrieder, S. Cheng, J. Li, *Adv. Funct. Mater.* **2022**, *32*, 2108773.

[38] S. Park, H. Lee, Y. Kim, P. S. Lee, *NPG Asia Mater.* **2018**, *10*, 959.
[39] H. Chen, S. Chen, Y. Zhang, H. Ren, X. Hu, Y. Bai, *ACS Appl. Mater. Interfaces* **2020**, *12*, 56319.
[40] B. Asbani, B. Bounor, K. Robert, C. Douard, L. Athouël, C. Lethien, J. L. Bideau, T. Brousse, *J. Electrochem. Soc.* **2020**, *167*, 100551.
[41] J. Yun, H. Lee, C. Song, Y. R. Jeong, J. W. Park, J. H. Lee, D. S. Kim, K. Keum, M. S. Kim, S. W. Jin, Y. H. Lee, J. W. Kim, G. Zi, J. S. Ha, *Chem. Eng. J.* **2020**, *387*, 124076.
[42] H. S. Min, B. Y. Park, L. Taherabadi, C. Wang, Y. Yeh, R. Zaouk, M. J. Madou, B. Dunn, *J. Power Sources* **2008**, *178*, 795.
[43] Y. Zeng, Y. Meng, Z. Lai, X. Zhang, M. Yu, P. Fang, M. Wu, Y. Tong, X. Lu, *Adv. Mater.* **2017**, *29*, 1.
[44] L. He, T. Hong, X. Hong, X. Liao, Y. Chen, W. Zhang, H. Liu, W. Luo, L. Mai, *Energy Technol.* **2019**, *7*, 1.
[45] M. Kotobuki, Y. Suzuki, H. Munakata, K. Kanamura, Y. Sato, K. Yamamoto, T. Yoshida, *Electrochim. Acta* **2011**, *56*, 1023.